Journal of
Materials Chemistry A

PAPER

View Article Online
View Journal | View Issue

Cite this: J. Mater. Chem. A, 2014, 2, 637

# Band gap engineered $TiO_2$ nanoparticles for visible light induced photoelectrochemical and photocatalytic studies†

Mohammad Mansoob Khan,[a] Sajid A. Ansari,[a] D. Pradhan,[b] M. Omaish Ansari,[a] Do Hung Han,[a] Jintae Lee[a] and Moo Hwan Cho*[a]

Received 9th October 2013
Accepted 29th October 2013

DOI: 10.1039/c3ta14052k

www.rsc.org/MaterialsA

Visible light-active $TiO_2$ (m-$TiO_2$) nanoparticles were obtained by an electron beam treatment of commercial $TiO_2$ (p-$TiO_2$) nanoparticles. The m-$TiO_2$ nanoparticles exhibited a distinct red-shift in the UV-visible absorption spectrum and a much narrower band gap (2.85 eV) due to defects as confirmed by diffuse reflectance spectroscopy (DRS), photoluminescence (PL), X-ray diffraction, Raman spectroscopy, electron paramagnetic resonance, transmission electron microscopy, X-ray photoelectron spectroscopy (XPS), electrochemical impedance spectroscopy (EIS) and linear scan voltammetry (LSV). The XPS revealed changes in the surface states, composition, $Ti^{4+}$ to $Ti^{3+}$ ratio, and oxygen deficiencies in the m-$TiO_2$. The valence band XPS, DRS and PL results were carefully examined to understand the band gap reduction of m-$TiO_2$. The visible light-responsive enhanced photocatalytic activity of m-$TiO_2$ was demonstrated by degrading methylene blue and brilliant blue G. The EIS and LSV in the dark and under visible light irradiation further support the visible light-induced photocatalytic activities of the m-$TiO_2$ due to a decrease in electron transfer resistance and an increase in photocurrent. This study confirms that m-$TiO_2$ can be used effectively as a photocatalyst and photoelectrode material owing to its enhanced visible light-induced photocatalytic activity.

## 1. Introduction

Nanocrystalline transition metal oxides have attracted considerable attention because of their potential applications in a range of processes, and are expected to be the key materials for further developments of science and technology.[1] Among the metal oxides available, $TiO_2$ has attracted particular attention owing to its exceptional properties, such as low cost, high stability, high chemical inertness, biocompatibility, non-toxicity, *etc.*[1–3] $TiO_2$ has been examined widely as an efficient photocatalyst for purification of water, and degradation of dyes, pesticides, *etc.* since the discovery of its photocatalytic properties by Honda–Fujishima.[1–5] On the other hand, $TiO_2$ is virtually inactive in visible light owing to its wide band gap (~3.2 eV). Therefore, band gap engineering by possible modification of materials is one of the exciting research areas.

Recently, many strategies have been adopted to develop visible light active $TiO_2$ as a photocatalyst, which includes non-metal doping,[6–10] metal doping,[10–13] reduced $TiO_2$,[14] self-doping or defect engineering.[15,16] Among the techniques available, electron beam (EB)-assisted nanofabrication and modification is exciting because it does not involve the use of hazardous chemicals and is considered relatively green compared to other reported methodologies.[17–19] In the case of EB irradiation under ambient conditions, the interaction of highly reactive electrons with air molecules is expected to give rise to highly reactive and strong oxidizing agents, such as ozone, OH groups or other radicals, which can react further with $TiO_2$ nanoparticles.[17,18] The interaction of $TiO_2$ with the high energy electrons generated by EB and oxidizing agents/ozone can result in the reduction of $Ti^{4+}$ to $Ti^{3+}$, or the formation of oxygen deficient/rich species.[19] Therefore, it is expected that a wide range of metal oxides with different properties depending on the electron beam intensity/exposure time, *etc.* can be prepared due to the large number of reaction possibilities.[17–21]

In this study, an electron beam was used for band gap engineering to decrease the band gap of $TiO_2$ nanoparticles without using any dopants because it is quite simple and the reproducibility is also very high. Modified $TiO_2$ (m-$TiO_2$) nanoparticles showed a remarkable decrease in the band gap as well as enhanced optical properties, thereby enhancing their photocatalytic activities in visible light ($\lambda$ > 500 nm). m-$TiO_2$

---

[a] *School of Chemical Engineering, Yeungnam University, Gyeongsan-si, Gyeongbuk 712-749, South Korea. E-mail: mhcho@ynu.ac.kr; Fax: +82-53-810-4631; Tel: +82-53-810-2517*

[b] *Materials Science Centre, Indian Institute of Technology, Kharagpur, W. B., 721302, India*

† Electronic supplementary information (ESI) available: Diffuse absorbance spectra, EPR spectra and XPS spectra of p-$TiO_2$ and m-$TiO_2$ nanoparticles. See DOI: 10.1039/c3ta14052k

nanoparticles exhibited an excellent visible light-induced photo-degradation response towards methylene blue (MB) and brilliant blue G (BB) degradation, which was not possible for p-$TiO_2$ under similar conditions. Electrochemical impedance spectroscopy (EIS) and linear scan voltammetry (LSV) further support the visible light-induced photocatalytic activities of m-$TiO_2$ nanoparticles due to a decrease in the electron transfer resistance and an increase in photocurrent under visible light irradiation. This study confirmed that the band gap engineered m-$TiO_2$ nanoparticles could be used effectively as photocatalysts and photoelectrode materials owing to their enhanced visible light photocatalytic activities. The proposed methodology is simple, does not involve the use of chemicals and doping agents, such as metals, non-metals, capping agents, *etc.*, and has great potential applications on a commercial scale.

## 2. Experimental

### 2.1. Materials

$TiO_2$ nanoparticles (size < 25 nm), MB and BB were purchased from Sigma-Aldrich. Sodium sulphate was obtained from Duksan Pure Chemicals Co. Ltd., South Korea. Ethyl cellulose and α-terpineol were supplied by KANTO Chemical Co., Japan and fluorine-doped transparent conducting oxide glass (FTO; F-doped $SnO_2$ glass; 7 Ω $sq^{-1}$) was acquired from Pilkington, USA. All chemicals were of analytical grade and used as received. Deionized water was prepared using a PURE ROUP 30 water purification system.

### 2.2. Methods

An EB accelerator (ELV-0.5, BINP, Russia), with a maximum beam power, maximum beam current and maximum beam energy of 28 kW, 40 mA and ~0.7 MeV, respectively, was used to modify p-$TiO_2$. UV-vis diffuse reflectance/absorbance spectroscopy (DRS) of the powdered p-$TiO_2$ and m-$TiO_2$ nanoparticles was performed using a UV-VIS-NIR double beam spectrophotometer (VARIAN, Cary 5000, USA) equipped with a diffuse reflectance accessory. A He–Cd laser (Kimon, 1 K, Japan) with a wavelength of 325 nm and a power of 50 mW was used as the excitation source for the photoluminescence (PL) measurements. X-ray diffraction (XRD, PANalytical, X'pert PRO-MPD, The Netherlands) was performed using Cu Kα radiation ($\lambda$ = 0.15405 nm). Raman spectroscopy was performed on a HR800 UV Raman microscope (Horiba Jobin-Yvon, France). The electron paramagnetic resonance (EPR) measurements were performed using a Bruker EMX system. X-ray photoelectron spectroscopy (XPS, ESCALAB 250 XPS System, Thermo Fisher Scientific U.K.) was conducted with the following X-ray source: monochromated Al Kα, $h\nu$ = 1486.6 eV, X-ray energy: 15 kV, 150 W and spot size: 500 μm. The XP spectra were fitted using the "Avantage program". The microstructures of the p-$TiO_2$ and m-$TiO_2$ were observed by high resolution transmission electron microscopy (HRTEM, JEM-2100 JEOL) at an operating voltage of 200 kV. The selected-area electron diffraction (SAED) images were recorded by HRTEM. The photocatalytic degradation and photoelectrochemical experiments (EIS and LSV) were conducted using a 400 W lamp with an irradiating intensity of 31.0 mW $cm^{-2}$ (3M, USA). The EIS and LSV measurements were carried out using a potentiostat (Versa STAT 3, Princeton Research, USA) with a standard three-electrode system, in which Ag/AgCl (saturated with KCl), a Pt gauge and fluorine-doped tin oxide (FTO) glass coated with p-$TiO_2$, or m-$TiO_2$ were used as the reference, counter and working electrodes, respectively, in a 0.2 M $Na_2SO_4$ solution as the electrolyte. The working electrodes for EIS and LSV were prepared as follows: 100 mg of each sample was suspended thoroughly by adding ethyl cellulose as a binder and α-terpineol as a solvent for the paste, and then coated on a FTO glass electrode using the doctor-blade method.

### 2.3. Electron beam modification of $TiO_2$ nanoparticles

Commercial $TiO_2$ nanoparticles were modified using an EB accelerator in integral mode with an EB energy of 0.7 MeV and an initial EB current of 2 mA $s^{-1}$ in water at room temperature under atmospheric pressure. A 75 mL aqueous dispersion of p-$TiO_2$ (50 mM) was prepared. The initial pH of the aqueous dispersions was 4.40. The final pH of the aqueous dispersion became 3.65 when exposed to an EB dose of 90 kGy (power 2724 mA s and real time 23.40 minute). The almost white p-$TiO_2$ changed to light pale yellow upon EB exposure at a dose of 90 kGy. The resulting dispersion was centrifuged and a yellowish-white powder was obtained; it was dried in an oven at 105 °C and then used for different characterization techniques and applications.

### 2.4. Photoelectrochemical studies of the p-$TiO_2$ and m-$TiO_2$ nanoparticles

To examine the photoelectrode response of the p-$TiO_2$ and m-$TiO_2$ nanoparticles, photoelectrochemical experiments, such as EIS and LSV, were conducted under ambient conditions in the dark and under visible light irradiation in a 50 mL 0.2 M $Na_2SO_4$ aqueous solution at room temperature. For each electrode, EIS was first performed under dark conditions, and later under visible light irradiation ($\lambda$ > 500 nm) at 0.0 V and with a frequency ranging from 1 to $10^4$ Hz. The photocurrent response was obtained by LSV in the dark and under visible light irradiation at a scan rate of 50 mV $s^{-1}$ over the potential range of −1.0 to 1.0 V.

### 2.5. Photocatalytic degradation of MB and BB by p-$TiO_2$ and m-$TiO_2$ nanoparticles

The photocatalytic activities of the p-$TiO_2$ and m-$TiO_2$ nanoparticles were tested for the catalytic degradation of MB (10 mg $L^{-1}$) as well as BB (10 mg $L^{-1}$) and estimated, as reported earlier.[12,15] For the photodecomposition experiment, 2 mg of each photocatalyst was suspended in 20 mL of the MB and BB aqueous solutions. Each solution was sonicated for 5 min and later stirred in the dark for 30 min to complete the adsorption and desorption equilibrium of the specific substrate on the p-$TiO_2$ and m-$TiO_2$ nanoparticles. The solutions were irradiated using a 400 W lamp ($\lambda$ > 500 nm). The two sets of experiments for MB and BB degradation were observed for 7 h and 5 h, respectively. The rate of MB and BB degradation was examined by taking 2 mL of the samples from each set every 1 h, centrifuging them to remove the catalyst and recording the UV-vis spectra, from which the degradation rate of MB and BB was calculated.

As a control experiment, p-$TiO_2$ nanoparticles (reference photocatalyst, Sigma-Aldrich) were used to degrade MB and BB under the same experimental conditions. Each degradation experiment was performed in triplicate to ensure the photocatalytic activity of the p-$TiO_2$ and m-$TiO_2$ nanoparticles. The stability and reusability of the m-$TiO_2$ nanoparticles were also tested in a similar manner to that mentioned above.

## 3. Results and discussion

In the modification process, EB is used as a "defect engineer", which can create a range of defects or modification in the $TiO_2$ nanoparticles, thereby imparting novel characteristics, such as reduced band gap and visible light induced photocatalytic activities. This protocol does not involve any expensive or toxic chemicals, which make this modification method highly economical, useful and efficient in the field of nanoparticle modification. The complete synthesis took place in water at room temperature under atmospheric pressure. Fig. 1 presents the suggested mechanism for the modification of commercially available $TiO_2$ nanoparticles by EB, which is economical, simple and efficient. The EB-assisted high energy electrons can either interact with some of the $Ti^{4+}$ ions and reduced them to $Ti^{3+}$ or interact with water molecules and air, and may form solvated electrons and strong oxidizing agents, such as ozone ($O_3$) and OH groups, which can alter the $TiO_2$ composition.[17–21] The *in situ* generated species, such as solvated electrons, OH, $\dot{O}_2$, *etc* and $Ti^{3+}$ ions formed by EB might modify the commercial $TiO_2$ nanoparticles and impart enhanced visible light induced photocatalytic activities to m-$TiO_2$.[22,23]

### 3.1. Optical properties of the p-$TiO_2$ and m-$TiO_2$ nanoparticles

EB irradiation of the $TiO_2$ nanoparticles leads to surface defects. Therefore, a change in the catalytic and chemical properties is predictable. Fig. 2(a) presents the absorbance and reflectance spectra of p-$TiO_2$ and m-$TiO_2$ (Fig. S1, ESI,† the inset shows the color of the samples). A significant red shift in the absorbance of m-$TiO_2$ was observed, which was attributed to band gap shifting. The tangent drawn shows an absorbance maxima of ~395 nm and ~430 nm for the p-$TiO_2$ and m-$TiO_2$ nanoparticles, respectively, which corresponds to a band gap of 3.15 and 2.85 eV, respectively. This suggests that $e^-$–$h^+$ pairs can be generated, even though the particle is irradiated with long wavelength-visible light.[15] This also suggests that the optical band gap of the m-$TiO_2$ nanoparticles has been reduced substantially compared to p-$TiO_2$. The decrease of band gap can be due to the localized gap states induced by $Ti^{3+}$.[15,22,23] The decrease in band gap has also been attributed to oxygen vacancies, which is responsible for the unique properties for photocatalytic applications.[23] Because band gap narrowing is directly proportional to the photocatalytic activity, m-$TiO_2$ nanoparticles are expected to show more activity in the visible region of the electromagnetic spectrum. Therefore, m-$TiO_2$ was used for dye degradation and photoelectrodes under visible light irradiation.

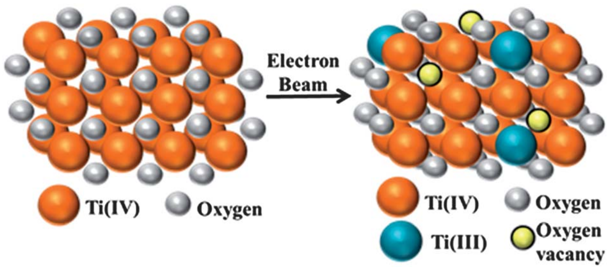

Fig. 1 Proposed mechanism for the modification of commercially available $TiO_2$ nanoparticles by EB.

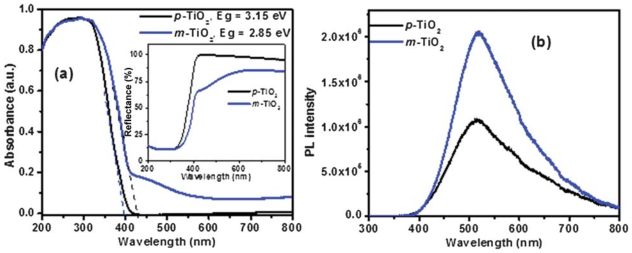

Fig. 2 (a) UV-vis diffuse absorbance spectra of the p-$TiO_2$ and m-$TiO_2$ nanoparticles showing the direct band gap measurements and the inset shows their UV-vis diffuse reflectance spectra, and (b) PL spectra of the p-$TiO_2$ and m-$TiO_2$ nanoparticles.

### 3.2. PL spectra of the p-$TiO_2$ and m-$TiO_2$ nanoparticles

PL is used primarily to determine the effectiveness of trapping, migration and transfer of charge carriers, as well as to understand the fate of the $e^-$–$h^+$ pairs in semiconductors.[24] In this study PL is used to understand the optical properties, surface states, oxygen vacancy and defects of the p-$TiO_2$ and m-$TiO_2$ nanoparticles. In general metal doped metal-oxides show low PL intensities compared to metal oxides.[12,25–28] However, the m-$TiO_2$ nanoparticles showed high PL intensities compared to the p-$TiO_2$ (Fig. 2(b)). This was attributed to the presence of either oxygen vacancies and/or defects in m-$TiO_2$ nanoparticles, which leads to an increase in their optical properties. Oxygen vacancies and defects were reported to bind the photo-induced electrons easily to form excitons, so that the PL signal can occur easily. Therefore, the PL signal increased with the increasing content of oxygen vacancies or defects.[29–31] Therefore, the high intensity of the PL spectrum for the m-$TiO_2$ nanoparticles compared to p-$TiO_2$ was attributed to the high concentration of oxygen vacancies and other defects.[23,24,29–31] This observation is in accordance with the UV-vis absorbance spectra (Fig. 2(a)) and previous reports.[24–31]

### 3.3. XRD of the p-$TiO_2$ and m-$TiO_2$ nanoparticles

The XRD pattern showed strong XRD peaks for both m-$TiO_2$ and p-$TiO_2$, which suggests that the $TiO_2$ is crystalline in nature. The

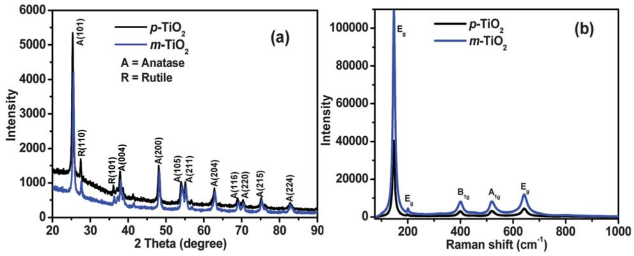

Fig. 3 (a) XRD patterns, and (b) Raman spectra of the p-$TiO_2$ and m-$TiO_2$ nanoparticles.

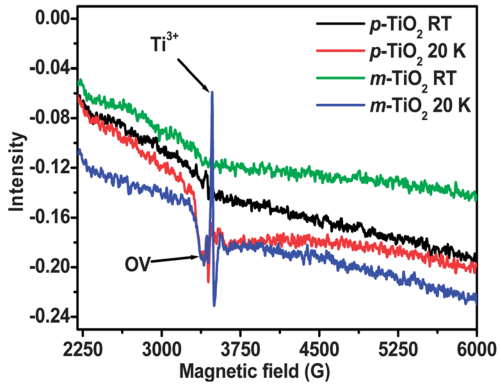

Fig. 4 EPR spectra of the p-$TiO_2$ and m-$TiO_2$ nanoparticles at room temperature and 20 K.

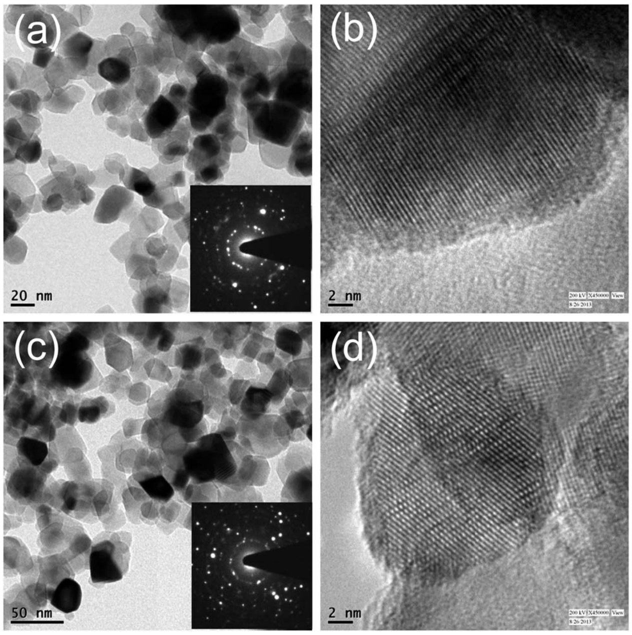

Fig. 5 TEM images of p-$TiO_2$ (a) and m-$TiO_2$ (c); HRTEM images of p-$TiO_2$ (b) and m-$TiO_2$ nanoparticles (d). The insets in (a) and (c) show the corresponding selected area electron diffraction pattern.

XRD pattern shows the prominent diffraction peaks for the planes of $TiO_2$ (anatase and rutile phase). The XRD pattern of m-$TiO_2$ nanoparticles was similar to that of p-$TiO_2$ except for a minor difference in the peak intensities. The slight decrease in the intensity of the m-$TiO_2$ nanoparticles might be due to defects and surface modification of $TiO_2$.[22] No obvious signs of any impurity were detected by XRD. This shows that after EB irradiation, the basic structure of $TiO_2$ has not changed, even though the slight decrease in the intensity of the m-$TiO_2$ nanoparticles indicates a small decrease in the crystallinity of the m-$TiO_2$ nanoparticles. The mean crystallite size of the p-$TiO_2$ and m-$TiO_2$ nanoparticles was calculated using the Scherrer formula, $D = \kappa\lambda/\beta\cos\theta$, where $\kappa$ is the shape factor and has a typical value of 0.9, $\lambda$ is the wavelength of the X-rays (Cu $K\alpha = 0.15405$ nm), $\beta$ is the full width at half maximum (FWHM) of the most intense peak, and $\theta$ is the peak position.[32] Using this equation, the calculated crystallite sizes of the p-$TiO_2$ and m-$TiO_2$ nanoparticles at $\sim$25.5° $2\theta$ were approximately 21.2 nm and 21.6 nm, respectively, which are within the range of the particle sizes measured by TEM (Fig. 5). After irradiation with 90 kGy EB, the crystallite size increased slightly. The increase in crystallite size upon EB irradiation indicates the formation of an amorphous phase and defects at the surface of $TiO_2$ nanoparticles. Similar changes were observed after the EB treatment of $TiO_2$.[17]

### 3.4. Raman spectra of the p-$TiO_2$ and m-$TiO_2$ nanoparticles

Raman spectroscopy was used to examine the structural changes in p-$TiO_2$ after EB irradiation. The anatase $TiO_2$ crystal normally shows six Raman active modes with frequencies of approximately 146 ($E_g$), 197 ($E_g$), 399 ($B_{1g}$), 515 ($A_{1g}$), 519 ($B_{1g}$, superimposed with the $A_{1g}$ band), and 639 cm$^{-1}$ ($E_g$).[7,23] m-$TiO_2$ displayed the typical Raman bands but they were broader (Fig. 3(b)). The FWHM of the most prominent $E_g$ band at $\sim$146 cm$^{-1}$ for p-$TiO_2$ and m-$TiO_2$ was measured to be 9.03 and 9.94 cm$^{-1}$, respectively. The broadening of the Raman peaks of m-$TiO_2$ was assigned to structural changes occurring in p-$TiO_2$ after EB irradiation, resulting in oxygen vacancies, various defects or the formation of $Ti^{3+}$ centers.[7,23]

### 3.5. EPR spectra of the p-$TiO_2$ and m-$TiO_2$ nanoparticles

The EPR spectra were recorded at room temperature (RT) and 20 K to confirm the presence of $Ti^{3+}$ ions (Fig. 4) and hence the paramagnetic nature of m-$TiO_2$. p-$TiO_2$ and m-$TiO_2$ at RT did not show any EPR signals, whereas the EPR signal was obvious at 20 K. The EPR signal from m-$TiO_2$ at 20 K was much stronger than that from p-$TiO_2$ with a $g$ value of 1.97 (for m-$TiO_2$) and 1.95 (for p-$TiO_2$). The observed $g$ value (Fig. S2, ESI†) matched the characteristics of the paramagnetic $Ti^{3+}$ ion center in a distorted rhombic oxygen ligand field.[15,22,23,33,34] Both p-$TiO_2$ and m-$TiO_2$ showed another EPR signal at 20 K, which corresponds to oxygen vacancies (OV).[23] Therefore, EPR revealed m-$TiO_2$ to have stronger paramagnetic character and a larger number of OV, which enhances the visible light photocatalytic activity.[22,23,33]

### 3.6. Microstructure of the p-$TiO_2$ and m-$TiO_2$ nanoparticles

Fig. 5 shows TEM images of the p-$TiO_2$ and m-$TiO_2$ nanoparticles. The size of the nanoparticles was in the range of 15 to 30 nm, from the bright-field TEM images in accordance with XRD analysis. The spot selected area electron diffraction pattern [shown in the inset of Fig. 5(a) and (c)] and continuous lattice [Fig. 5(b) and (d)] confirmed the crystalline nature of the $TiO_2$ nanoparticles. The measured lattice spacing of 0.37 nm matched the distance between the {101} planes of the anatase $TiO_2$ crystal. The reflection from the same {101} plane was prominent in the XRD patterns (Fig. 3) of these nanoparticles. Interestingly, the outer edge of these nanoparticles appeared blurry [Fig. 5(b) and (d)], indicating an amorphous or disorder phase on the nanoparticle surface. Moreover, TEM of the p-$TiO_2$ and m-$TiO_2$ nanoparticles revealed no distinct change in crystallinity.

### 3.7. XP spectra of p-$TiO_2$ and m-$TiO_2$ nanoparticles

The surface characterization of p-$TiO_2$ and m-$TiO_2$ was performed by XPS. Carbon, oxygen and titanium were detected in the survey spectra (Fig. S3(a), ESI†). The C 1s photoelectron peak at a binding energy (BE) of 285 eV was stronger for p-$TiO_2$ than the m-$TiO_2$ nanoparticles, which was attributed to the removal of surface carbon impurities by EB irradiation (Fig. S3(b), ESI†). Fig. 6(a) shows the XP spectrum of p-$TiO_2$ in the Ti 2p binding energy (BE) region. The XPS Ti 2p peak can be deconvoluted into four Ti 2p peaks; $Ti^{3+}$ $2p_{3/2}$ at 457.31 eV, $Ti^{3+}$ $2p_{1/2}$ at 461.12 eV, $Ti^{4+}$ $2p_{3/2}$ at 459.20 eV, and $Ti^{4+}$ $2p_{1/2}$ at 464.93 eV. Similarly, Fig. 6(b) shows the XP spectrum of m-$TiO_2$ with four Ti 2p peaks, $Ti^{3+}$ $2p_{3/2}$ at 458.77 eV, $Ti^{3+}$ $2p_{1/2}$ at 462.76 eV, $Ti^{4+}$ $2p_{3/2}$ at 459.31 eV, and $Ti^{4+}$ $2p_{1/2}$ at 464.99 eV.[7,20,35] Both Ti $2p_{3/2}$ and Ti $2p_{1/2}$ peaks exhibited a significant change after EB irradiation. In particular, the $Ti^{4+}$ concentrations decreased with EB irradiation, whereas the $Ti^{3+}$ concentrations increased. The amount of $Ti^{3+}$ on the $TiO_2$ surface plays an important role, as reported in the case of $TiO_2$ doped with metal atoms. The photogenerated electrons can be trapped in $Ti^{3+}$, thereby inhibiting the recombination of majority and minority carriers.[35]

To determine the binding states of oxygen in p-$TiO_2$ and m-$TiO_2$, the O 1s XPS peak was fitted to three peaks (Fig. 6(b) and (d)) centered at 530.52, 532.22 and 528.06 eV for p-$TiO_2$ and 530.62, 531.92 and 529.68 eV for m-$TiO_2$.[7,20,35] The shift in the O 1s BE of m-$TiO_2$ compared to p-$TiO_2$ indicates the change in the type of oxygen bonding, which is related to the formation of $Ti^{3+}$.[23] The photoelectron peak at approximately 530.62 and 529.68 eV could be assigned to the lattice oxygen in $TiO_2$ and $Ti_2O_3$, respectively, whereas the peak at 531.92 eV was assigned to water adsorbed on the $TiO_2$ surface. Because EB irradiation affects only the $TiO_2$ surface, the change from $Ti^{4+}$ to $Ti^{3+}$ was not detected by XRD (Fig. 3(a)). On the other hand, the reduction of $Ti^{4+}$ was clearly detected by XPS (Fig. 6).

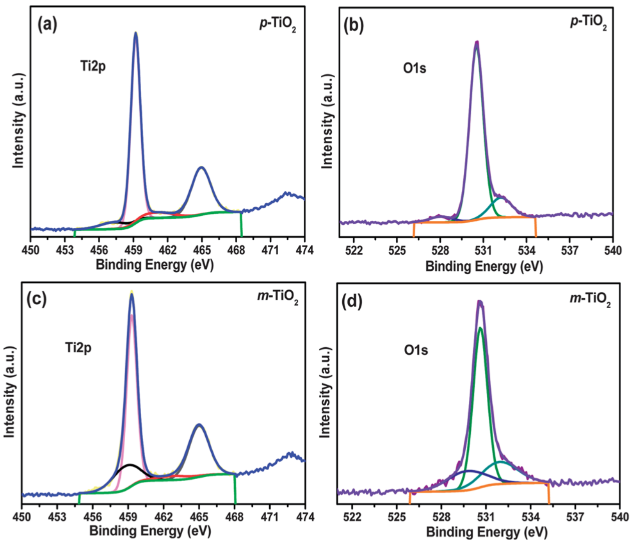

Fig. 6 Deconvoluted XP spectra of Ti 2p (a and c) and O 1s (b and d) for p-$TiO_2$ (a and b), and m-$TiO_2$ nanoparticles (c and d).

The band gap reduction could occur by the formation of mid gap band states either above the valence band (VB) or below the conduction band (CB) overlapping with the respective band. Therefore, VB XPS of the p-$TiO_2$ and m-$TiO_2$ nanoparticles was performed to examine the band gap narrowing phenomenon (Fig. 7(a)). The VB maximum of p-$TiO_2$ was observed at 1.65 eV, whereas the VB maximum of the m-$TiO_2$ was noted at 0.61 eV, showing a ∼1.04 eV shift to a lower binding energy.[7,30,36] This shift was assigned to surface oxygen vacancies and/or disorderliness in accordance with our TEM result and several other recent reports.[7,30,37] In particular Chen *et al.*[7] reported such an uplift of VB which was due to the presence of a disorder shell in the hydrogenated black $TiO_2$ nanoparticles. However, the band gap reduction due to lowering of CB was reported to be due to defects such as oxygen vacancies[30,38] and $Ti^{3+}$ formation, which is related to the oxygen vacancies.[30,36–39] The reduction of the m-$TiO_2$ band gap in the present work can therefore be attributed to both the uplift of VB (due to surface disorderliness) and lowering of CB (due to oxygen vacancies and $Ti^{3+}$ defect centers).[7,30,37–39]

A schematic illustration of the density of states (DOS) of the p-$TiO_2$ and m-$TiO_2$ nanoparticles is shown in Fig. 7(b) on the basis of VB XPS results (Fig. 7(a)). A measured band gap of 3.15 eV indicates negligible change in the band edges of p-$TiO_2$. The p-$TiO_2$ displayed typical VB DOS characteristics of $TiO_2$, with the edge of the maximum energy at about 1.65 eV. Therefore, the CB minimum would occur at about −1.50 eV. For the m-$TiO_2$, the VB maximum energy blue-shifts toward the vacuum level at ∼0.61 eV. A lower band gap from the DRS measurement for the m-$TiO_2$ and VB XPS shifts is obviously due to the surface disorder produced by EB irradiation. In addition, there may be CB tail states arising from the defects ($Ti^{3+}$) that extend below

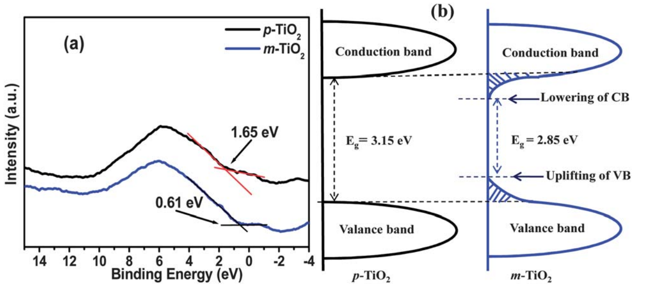

Fig. 7 (a) Valence band XPS spectra, and (b) the density of states for the p-$TiO_2$ and m-$TiO_2$ nanoparticles.

the conduction band minimum.[7,30,37–39] Optical transitions from the blue-shifted VB edge to these band tail states are presumably responsible for optical absorption in m-$TiO_2$. This assumption is supported further by DRS observations.

### 3.8. Photoelectrochemical studies and photocatalytic degradation of MB and BB by the p-$TiO_2$ and m-$TiO_2$ nanoparticles

EIS was performed on the p-$TiO_2$ and m-$TiO_2$ nanoparticles to examine the charge transfer resistance and separation efficiency between the photogenerated electrons and holes because the charge separation efficiency of photogenerated electrons and holes is a critical factor for the photocatalytic activity.[40,41] Fig. 8(a) shows typical EIS Nyquist plots of the p-$TiO_2$ and m-$TiO_2$ photocatalysts in the dark and under visible light irradiation. The arc radius of the EI spectra reflects the interface layer resistance arising at the surface of the electrode.[41] The smaller arc radius indicates higher charge transfer efficiency. The arc radius of the m-$TiO_2$ nanoparticles was smaller than that of p-$TiO_2$ in the cases of dark conditions and visible light irradiation. This suggests that the m-$TiO_2$ photocatalysts have lower resistance than that of p-$TiO_2$, which can accelerate the interfacial charge-transfer process. These observations support the DRS and PL results as well as the visible light-induced photocatalytic degradation results. EIS also supported the important role of $Ti^{3+}$ and different types of oxygen vacancies and other defects, which facilitate the charge separation and transfer efficiency of the photogenerated electrons and holes on the surface of the m-$TiO_2$ photocatalysts.[40,41]

The enhanced visible light photoactivity of the m-$TiO_2$ was examined by measuring the photocurrent using LSV in the dark and under visible light irradiation.[41,42] Fig. 8(b) shows the improvement in the photocurrent response of m-$TiO_2$, which was attributed to the increase in light harvesting ability due to the various types of defects, which give a narrower band gap compared to p-$TiO_2$. This helps to excite the valence electrons to the conduction band by absorbing visible light. The photo-electro-chemical activity was determined by both the ability of light-harvesting and the separation of $e^-/h^+$ pairs. Therefore, $e^-$–$h^+$ pairs are generated by absorbing the incident photons with energies larger than $E_g$, and they will recombine unless they are separated quickly.[43] Generally, a high photocurrent indicates that the sample has a strong ability to generate and transfer the photoexcited charge carriers under irradiation.[41–43] m-$TiO_2$ showed a higher photocurrent than p-$TiO_2$ under the same conditions, suggesting that m-$TiO_2$ exhibits a stronger ability for $e^-$–$h^+$ pair separation than p-$TiO_2$, which is supported by the PL spectra. The substantial improvement in the photocurrent for m-$TiO_2$ shows that it can be induced easily with visible light, and produce more photoinduced carriers, resulting in high visible photocatalytic activity. EIS and LSV showed that the m-$TiO_2$ nanoparticles can be used effectively as photocatalysts and photoelectrode materials.

MB is a hetero-polyaromatic model dye used in textile industries that is mildly toxic, whereas BB is also a polyaromatic dye used in biochemical analyses. The photocatalytic activities of the p-$TiO_2$ and m-$TiO_2$ nanoparticles to degrade MB and BB under the visible light ($\lambda > 500$ nm) were examined, as reported earlier.[15,40] The m-$TiO_2$ nanoparticles showed better photocatalytic degradation of MB and BB than p-$TiO_2$ (Fig. 9(a) and (b)). The photocatalytic degradation was estimated from the decrease in the absorption intensity of MB and BB at a fixed wavelength, $\lambda_{max} = 665$ nm and $\lambda_{max} = 595$ nm, during the course of the visible light photocatalytic degradation reaction. The degradation was calculated using the relationship, $C/C_0$, where $C_0$ is the initial concentration and $C$ is the concentration after photo-irradiation (Fig. 9(a) and (b)). The enhanced photocatalytic activity of the m-$TiO_2$ nanoparticles compared to p-$TiO_2$ can be explained by the surface modification and defects in m-$TiO_2$ nanoparticles. Oxygen vacancies, other defects and $Ti^{3+}$ centers enhance the photocatalytic activity.[15,23,44,45] The variation in the photocatalytic activity of p-$TiO_2$ and m-$TiO_2$ nanoparticles is also supported by DRS (Fig. 2(a)), EPR (Fig. 4), and XPS (Fig. 6 and 7). These results clearly show that the visible light photocatalytic activity of m-$TiO_2$ nanoparticles can be improved greatly by narrowing the band gap and forming various defects and $Ti^{3+}$ centers.[15,23,44,45]

From the above studies, discussion and proposed photocatalytic decomposition mechanism (Fig. 10), it is obvious that EB is an effective tool for narrowing the band gap of $TiO_2$, making it suitable for the decomposition of toxic chemicals and as a photoactive material for electrodes under visible light irradiation. The enhancement of the performance of m-$TiO_2$ was attributed to the high separation efficiency of $e^-$–$h^+$ pairs due to (Fig. 10) surface oxygen-vacancies and $Ti^{3+}$ formation which lead to band

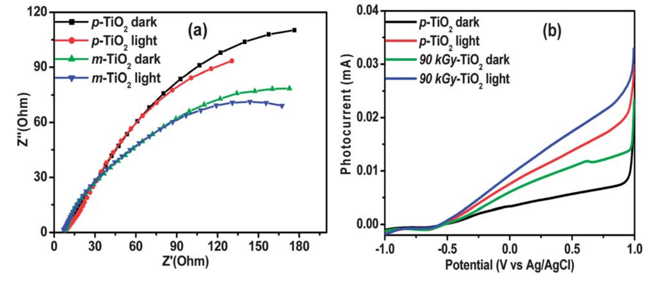

Fig. 8 (a) EIS (Nyquist plots), and (b) photocurrent response measured by LSV of the p-$TiO_2$ and m-$TiO_2$ nanoparticles in the dark and under visible light irradiation.

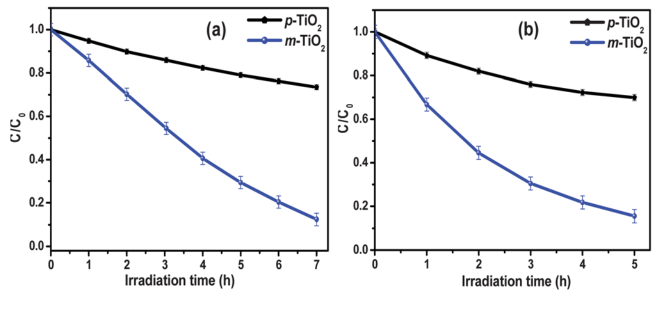

Fig. 9 Visible light photocatalytic degradation of (a) MB, and (b) BB by p-$TiO_2$ and m-$TiO_2$ nanoparticles.

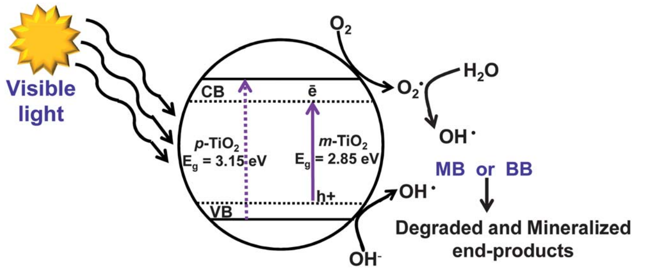

Fig. 10 Proposed mechanism for the degradation of MB and BB by the m-TiO$_2$ nanoparticles.

gap narrowing.[30,39,44,45] This narrowing of the band gap leads to visible light activity. Band gap excitation of the semiconductor results in $e^-$–$h^+$ separation. The high oxidative potential of the holes in the photocatalyst allows the formation of reactive intermediates. Reactive hydroxyl radicals ($^\bullet$OH) can be formed either by the decomposition of water or by the reaction of a hole with OH$^-$. The hydroxyl radicals and photogenerated holes are extremely strong, non-selective oxidants that lead to the degradation of MB and BB at the surface of the m-TiO$_2$ nanoparticles.[12,40] This can be attributed to the high concentration of oxygen vacancies, other defects and Ti$^{3+}$ centers created in the m-TiO$_2$ nanoparticles.[30,39,44,45] EIS and LSV further confirmed the visible light induced photoactivity of m-TiO$_2$. When commercially available TiO$_2$ (Sigma) was irradiated with 90 kGy EB, more defects formed or surface modification of TiO$_2$ occurred to make TiO$_2$ photoactive under visible light.

## 4. Conclusions

An electron beam was used to modify TiO$_2$ nanoparticles under ambient conditions, which results in an improvement in their visible light-induced photocatalytic activities. No structural changes occurred in m-TiO$_2$. On the other hand, surface defects, oxygen vacancy and Ti$^{3+}$ formation were identified. EIS and LSV in the dark and under visible light irradiation confirmed the visible light induced photoactivity of the m-TiO$_2$. Visible light induced photocatalytic degradation of MB and BB further confirmed the improved photoactivity of the m-TiO$_2$. This study suggests that m-TiO$_2$ can be used as a visible light active photocatalyst and photoelectrode material. The EB treatment can be used to prepare photoactive materials with enhanced visible light-induced photoactivity.

## Acknowledgements

This study was supported by the Basic Science Research Program through the National Research Foundation of Korea (NRF) funded by the Ministry of Education, Science and Technology (Grant no.: 2012R1A1A4A01005951).

## References

1 H. Chen, C. E. Nanayakkara and V. H. Grassian, *Chem. Rev.*, 2012, **112**, 5919–5948.

2 K. Hashimoto, H. Irie and A. Fujishima, *AAPPS Bull.*, 2007, **17**, 12–28.

3 M. Pelaez, N. T. Nolan, S. C. Pillai, M. K. Seery, P. Falaras, A. G. Kontos, P. S. M. Dunlop, J. W. J. Hamilton, J. A. Byrne, K. O'Sheaf, M. H. Entezari and D. D. Dionysiou, *Appl. Catal., B*, 2012, **125**, 331–349.

4 A. Fujishima and K. Honda, *Nature*, 1972, **238**, 37–38.

5 N. Roy, Y. Sohn and D. Pradhan, *ACS Nano*, 2013, **7**, 2532–2540.

6 R. Asahi, T. Morikawa, T. Ohwaki, K. Aoki and Y. Taga, *Science*, 2001, **293**, 269–271.

7 X. Chen, P. Y. Yu and S. S. Mao, *Science*, 2011, **331**, 746–750.

8 M. U. Khan, M. Al-shahry and W. B. Ingler Jr, *Science*, 2002, **297**, 2243–2245.

9 J. Yu, G. Dai, Q. Xiang and M. Jaroniec, *J. Mater. Chem.*, 2011, **21**, 1049–1057.

10 Y. Lin, Z. Jiang, C. Zhu, X. Hu, X. Zhang, H. Zhu, J. Fan and S. H. Lin, *J. Mater. Chem. A*, 2013, **1**, 4516–4524.

11 M. M. Khan, S. Kalathil, J. Lee and M. H. Cho, *Bull. Korean Chem. Soc.*, 2012, **33**, 1753–1758.

12 M. M. Khan, S. A. Ansari, J. Lee and M. H. Cho, *Nanoscale*, 2013, **5**, 4427–4435.

13 J. Yu, Y. Wang and W. Xiao, *J. Mater. Chem. A*, 2013, **1**, 10727–10735.

14 Q. Kang, J. Cao, Y. Zhang, L. Liu, H. Xu and J. Ye, *J. Mater. Chem. A*, 2013, **1**, 5766–5774.

15 S. Kalathil, M. M. Khan, S. A. Ansari, J. Lee and M. H. Cho, *Nanoscale*, 2013, **5**, 6323–6326.

16 S. Wendt, P. T. Sprunger, E. Lira, G. K. H. Madsen, Z. Li, J. Ø. Hansen, J. Matthiesen, A. B. Rasmussen, E. Lægsgaard, B. Hammer and F. Besenbacher, *Science*, 2008, **320**, 1755–1759.

17 M. J. Kim, K. D. Kim, W. S. Tai, H. O. Seo, Y. Luo, Y. D. Kim, B. C. Lee and O. K. Park, *Catal. Lett.*, 2010, **135**, 57–61.

18 K. D. Kim, W. S. Tai, Y. D. Kim, S. J. Cho, I. S. Bae, J. H. Boo, B. C. Lee, K. H. Yang and O. K. Park, *Bull. Korean Chem. Soc.*, 2009, **30**, 1067–1070.

19 K. D. Kim, W. S. Tai, Y. D. Kim, B. C. Lee, K. H. Yang and J. H. Park, *Surf. Interface Anal.*, 2010, **42**, 927–930.

20 J. Jum, J. H. Shin, J. S. Choi and M. Dhayal, *J. Biomed. Nanotechnol.*, 2006, **2**, 152–156.

21 H. O. Seo, C. W. Sim, K. D. Kim, Y. D. Kim, J. H. Park, B. C. Lee, K. H. Lee and D. C. Lim, *Radiat. Phys. Chem.*, 2012, **81**, 290–294.

22 X. Liu, S. Gao, H. Xu, Z. Lou, W. Wang, B. Huang and Y. Dai, *Nanoscale*, 2013, **5**, 1870–1875.

23 X. Pan, M. Q. Yang, X. Fu, N. Zhang and Y.-J. Xu, *Nanoscale*, 2013, **5**, 3601–3614.

24 J. Liqiang, Q. Yichun, W. Baiqi, L. Shudan, J. Baojiang, Y. Libin, F. Wei, F. Honggang and S. Jiazhong, *Sol. Energy Mater. Sol. Cells*, 2006, **90**, 1773–1787.

25 L. Jing, B. Xin, F. Yuan, L. Xue, B. Wang and H. Fu, *J. Phys. Chem. B*, 2006, **110**, 17860–17865.

26 J. Cao, B. Xu, B. Luo, H. Lin and S. Chen, *Catal. Commun.*, 2011, **13**, 63–68.

27 J. Hou, R. Cao, Z. Wang, S. Jiao and H. Zhu, *J. Mater. Chem.*, 2011, **21**, 7296–7301.

28 H. Liu, W. Cao, Y. Su, Y. Wanga and X. Wang, *Appl. Catal., B*, 2012, **111–112**, 271–279.

29 J. Wang, P. Liu, X. Fu, Z. Li, W. Han and X. Wang, *Langmuir*, 2009, **25**, 1218–1223.

30 A. Naldoni, M. Allieta, S. Santangelo, M. Marelli, F. Fabbri, S. Cappelli, C. L. Bianchi, R. Psaro and V. D. Santo, *J. Am. Chem. Soc.*, 2012, **134**, 7600–7603.

31 B. Santara, P. K. Giri, K. Imakita and M. Fujii, *J. Phys. Chem. C*, 2013, **117**, 23402–23411.

32 B. D. Cullity and S. R. Stock, *Elements of X-ray diffraction*, Prentice Hall, New Jersey, 2001.

33 F. Zuo, L. Wang, T. Wu, Z. Zhang, D. Borchardt and P. Feng, *J. Am. Chem. Soc.*, 2010, **132**, 11856–11857.

34 M. Chiesa, M. C. Paganini, S. Livraghi and E. Giamello, *Phys. Chem. Chem. Phys.*, 2013, **15**, 9435–9447.

35 H. B. Kim, D. W. Park, J. P. Jeun, S. H. Oh, Y. C. Nho and P. H. Kang, *Radiat. Phys. Chem.*, 2012, **81**, 954–957.

36 V. Etacheri, M. K. Seery, S. J. Hinder and S. C. Pillai, *Adv. Funct. Mater.*, 2011, **21**, 3744–3752.

37 T. Xia and X. Chen, *J. Mater. Chem. A*, 2013, **1**, 2983–2989.

38 Y. H. Hu, *Angew. Chem., Int. Ed.*, 2012, **51**, 12410–12412.

39 G. Yang, Z. Jiang, H. Shi, T. Xiao and Z. Yan, *J. Mater. Chem.*, 2010, **20**, 5301–5309.

40 S. A. Ansari, M. M. Khan, S. Kalathil, A. Nisar, J. Lee and M. H. Cho, *Nanoscale*, 2013, **5**, 9238–9246.

41 X. Bai, L. Wang, R. Zong, Y. Lv, Y. Sun and Y. Zhu, *Langmuir*, 2013, **29**, 3097–3105.

42 J. Gan, X. Lu, J. Wu, S. Xie, T. Zhai, M. Yu, Z. Zhang, Y. Mao, S. C. Wang, Y. Shen and Y. Tong, *Sci. Rep.*, 2013, **3**, 1021–1028.

43 W. Li, M. Li, S. Xie, T. Zhai, M. Yu, C. Liang, X. Ouyang, X. Lu, H. Li and Y. Tong, *CrystEngComm*, 2013, **15**, 4212–4216.

44 S. Livraghi, M. C. Paganini, E. Giamello, A. Selloni, C. D. Valentin and G. Pacchioni, *J. Am. Chem. Soc.*, 2006, **128**, 15666–15671.

45 Y. Lv, C. Pan, X. Ma, R. Zong, X. Bai and Y. Zhu, *Appl. Catal., B*, 2013, **138–139**, 26–32.